

# Detection of Einstein Telescope gravitational wave signals from binary black holes using deep learning

Wathela Alhassan,<sup>1\*</sup> T. Bulik,<sup>1,2</sup> M. Suchenek<sup>1</sup>

<sup>1</sup>*Particle Astrophysics Science and Technology Centre, Nicolaus Copernicus Astronomical Center, Rektorska 4, 00-614 Warsaw, Poland*

<sup>2</sup>*Astronomical Observatory, University of Warsaw, Aleje Ujazdowskie 4, 00-478 Warsaw, Poland*

Accepted XXX. Received YYY; in original form ZZZ

## ABSTRACT

The expected volume of data from the third-generation gravitational waves (GWs) Einstein Telescope (ET) detector would make traditional GWs search methods such as match filtering impractical. This is due to the large template bank required and the difficulties in waveforms modelling. In contrast, machine learning (ML) algorithms have shown a promising alternative for GWs data analysis, where ML can be used in developing semi-automatic and automatic tools for the detection and parameter estimation of GWs sources. Compared to second generation detectors, ET will have a wider accessible frequency band but also a lower noise. The ET will have a detection rate for Binary Black Holes (BBHs) and Binary Neutron Stars (BNSs) of order  $10^5 - 10^6 \text{ year}^{-1}$  and  $7 \times 10^4 \text{ year}^{-1}$  respectively. We explored the efficiency of using convolutional neural networks (CNNs) for the detection of BBHs' mergers in synthetic noisy data that was generated according to ET's parameters. Without performing data whitening or applying bandpass filtering, we trained four CNN networks with the state-of-the-art performance in computer vision, namely VGG, ResNet and DenseNet. ResNet has significantly better performance, and was able to detect BBHs sources with SNR of 8 or higher with 98.5% accuracy, and with 92.5%, 85%, 60% and 62% accuracy for sources with SNR range of 7-8, 6-7, 5-6 and 4-5 respectively. ResNet, in qualitative evaluation, was able to detect a BBH's merger at 60 Gpc with 4.3 SNR. It was also shown that CNN can be used efficiently for near-real time detection of BBHs.

**Key words:** gravitational waves - transients: black hole mergers - methods: data analysis

## 1 INTRODUCTION

The recent detection of Gravitational Waves (GWs) has opened a new era of multimessenger astrophysics, where significant amount of data is being delivered from the second generation detectors of GWs such as GEO600 (Willke 2007), the advanced Laser Interferometer Gravitational-Wave Observatory (LIGO) (Abbott et al. 2009), and the Virgo interferometer (Acernese et al. 2007).

The detection of GW signals is traditionally done through the analysis of a hidden signal in the raw data from the detector, so-called matched filtering. Matched filtering process compares modelled waveform templates with the raw data. The main disadvantage of match filtering is that it depends entirely on the availability of waveform templates. This process is computationally challenging, and depends also on the accuracy of the modelled waveforms. Once a signal is detected, the subsequent step is to estimate its parameters, for which as many as  $10^7$  waveform templates are required for an accurate estimation (Schmidt et al. 2020).

With the expected volume of data from the third generation GWs detectors such as the Einstein Telescope (ET) (Punturo et al. 2010; Abernathy et al. 2011; Maggiore

et al. 2020), Cosmic Explorer (CE) (Evans et al. 2021) and The Laser Interferometer Space Antenna (LISA) (Shaddock 2008), match filtering can be extremely computational expensive and the large template bank required would make it impractical. This motivates the necessity for the development of semi-automatic and automatic machine learning algorithms for detection, denoising and parameter estimation of GWs sources. Deep Learning (DL) is a promising alternative for GW data analysis, both for detection and parameter estimation. This goes back to its flexibility in categorizing and modelling patterns read from data, with very little human input. In contrast to match filtering search method, DL models can learn to distinguish between only noise and injected noise (noise plus signal) without the need to model every possible GW waveform. This is done through learning the underlying features of pure noise and injected noise, which gives DL an advantage over the traditional methods, where no matching is involved. DL algorithms can open up a new door for unmodelled waveforms discovery, specially with the expected number and type of sources that are expected to be detectable from the third generation detectors.

The ET will revolutionise the field of GWs in every sense, including and most importantly the better sensitivity of one order of magnitude that will provide, which will allow the detection at lower frequency. Compared to second generation

\* E-mail: wathelahamed@gmail.com

detectors, ET will have a wider accessible frequency band that can be used to investigate a huge number of key issues related to astrophysics, fundamental physics and cosmology. The ET will have a detection rate for BBHs and BNSs of order  $10^5 - 10^6 \text{ year}^{-1}$  and  $7 \times 10^4 \text{ year}^{-1}$  respectively (Kalogera et al. 2021). A recent study showed that, the BBHs would have lower detection rate at ET, which expected to be in the range  $3.1 \times 10^4$  to  $8.0 \times 10^4 \text{ year}^{-1}$  (Iacovelli et al. 2022). Our work here will focus on BBHs sources, and BNSs will be included in future work.

Over the last few years, different Machine Learning (ML) and DL techniques have been successfully applied to astronomical applications, on both images and spectral data (Lukic & Brüggén 2016). For example distinguishing between normal and peculiar optical galaxies by training Artificial Neural Networks (ANNs) (Naim et al. 1997). Estimation of the photometric redshift of galaxies using ANNs (Collister & Lahav 2004), improved methods of the estimation of the photometric redshift of galaxies with more accurate results (Zhang et al. 2009; Bonfield et al. 2010) and most recent improvement by D’Isanto & Polsterer (2018). Selim et al. (2016) and Selim & Abd El Aziz (2017) where a method based on non-negative matrix factorization algorithm were used to classify the galaxy morphology. Similar method has also been applied to the galaxy-star classification (Kim & Brunner 2017), and Radio sources classification using CNNs Alhassan et al. (2018).

In GW, ML and DL have been wildly introduced into the field of GW data analysis in recent years. For second generation detectors ML and DL techniques have been successfully applied on both, time and frequency domain GWs data. For example, ML was used for glitches identification (Colgan et al. 2020). Biswas et al. (2013) used artificial neural networks, support vector machines, and random forests on LIGO data for the identification and removal of glitches. Another successful application used ML to discover the correlation between auxiliary monitoring channels and the main GWs output channels, for improving the the sensitivity of the current interferometric GWs detectors (Vajente 2022). The potential of time-domain noise subtraction for improving detectors sensitivity below 30 Hz was also discussed in the paper. Baltus et al. (2021) used CNNs for pre-merger alert of three classes of BNSs of LIGO. This work was improved in (Baltus et al. 2022) to be able to search for all types of BNSs pre-mergers in three different types of noise: Gaussian O3 noise, real O3 noise, and predicted O4 noise. Moreno et al. (2022) used deep recurrent autoencoders (AEs) -with an unsupervised strategy- for GWs signals detection in laser interferometers. The results were better compared to other AEs architectures, but less accurate compared to the traditional supervised techniques. Álvarez et al. (2021) Used CNNs for BBHs merger detection from simulated data of a single detector (Advanced LIGO detector) and multi-detectors combined. Their models were trained on sources with luminosity distance ( $D_L$ ) ranging from 100 to 2000 Mpc, and masses between 5 to 100  $M_\odot$ . Results from model trained on single detector data and multi-detector data achieved an accuracy of 72% and 82% respectively. Similar work was done by Jiang et al. (2022), where CNNs was used to search the LIGO O1, O2 and O3 data for BBHs sources that have been detected by both, Hanford and Livingston detectors, using time sliding

method. Their model was able to detect the whole 41 BBHs sources exist in the data.

Detection of Extreme mass ratio inspirals (EMRIs) can be possible from third generation space-borne GW detectors such as LISA. A proof-of-principle approach for EMRI detection based on CNNs was presented in (Zhang et al. 2022), where their CNNs model was able to detect effectively EMRI systems with a signal-to-noise ratio (SNR) larger than 50. it has also been showed that, the CNNs’ performance is strongly associated with SNR.

ET is expected to have a detection horizon for BBHs up to redshift  $z = 100$ , but BBHs with total mass 20 - 100  $M_\odot$  will be visible up to  $z \approx 20$  (Singh et al. 2021). In this work, we focus on the detection of BBHs merger from the ET with luminosity distance up to 120 Gpc and component masses ranging from 15 to 56  $M_\odot$ . Different state-of-the-art CNNs models in image classification were used to find the most optimal performing model. Time-frequency domains of pure noise and injected noise have been used to train, validate and test our models.

The structure of this work goes as follow: in Section 2 we describe the method and tools were used for the generation of our synthetic data and the preprocessing pipeline employed for spectrograms preparation. Section 3 discusses The Convolutional Neural Networks, the DL networks used, and training and evaluation processes. Evaluating the best performing model on five hours of ET synthetic data is presented in section 4. Finally, a summary of this work and a future work plans is presented in Section 5.

## 2 ET DATASET GENERATION

Deep learning algorithms are data-hungry algorithms. This means they required a vast amount of data in order to generalize well. In our case -supervised classification- we have to provide thousands of samples to train and evaluate the algorithm. Our main task is to train different DL models, on frequency-time domain representations of only noise and injected noise, to be able to distinguish between the noise with a presence of GWs and without.

Time-frequency analysis, which is the prevalent method in distinguishing between GWs signal and noise, was used in the GWs discovery in finding the ‘chirp’ signal (Abbott et al. 2016). In this work, we use time-frequency domain (spectrograms) for the detection of GWs analysis, using The Short Time Fourier Transform (STFT). STFT is one of the most commonly used time-frequency transform for nonstationary signal analysis, known for its simplicity and efficiency, and it was also used in the current data analysis pipeline of LIGO (Klimenko et al. 2016). STFT was first introduced by Dennis Gabor in 1946, and it can mathematically be represented for a signal  $x(t)$  as:

$$X(\tau, \omega) = \int_{-\infty}^{\infty} x(t)w(t - \tau)e^{-i\omega t}d(t)$$

Where  $w$  is the window function,  $\tau$  and  $\omega$  are the time and frequency axis respectively. Choosing a window size is critical for the time-frequency resolution when using STFT (Yin et al. 2013). The main challenge in choosing a window size is the time-frequency localization trade-off (i.e. smaller window

size will result in a better temporal resolution but lower frequency resolution). Through experiments, as a window, we chose *blackman* window (Blackman & Tukey 1958) -which was designed to have the minimal possible spectral leakage that's linked to STFT- with a length of 1024 and 50% overlap resulting in a 62.5 ms temporal resolution. Figure 2 shows samples of the generated spectrograms.

ET is expected to observe individual sources, overlapped sources as well as stochastic background. We considered here only individual sources with no spinning. LALSsimulation through pyCBC python package (Nitz et al. 2022), using a single detector of the proposed ET telescope, was used for the generation of our GWs signals of BBHs and noise according to the ET's parameters. Combining data from different detectors can significantly improve the detection performance, compared to using a single detector as shown previously in (Álvarez et al. 2021). We expect that, using all ET's three detectors would significantly improve the performance of our models, and this will be tried in future work.

Generation of ET's noise using pyCBC incorporates two steps; the first step is the generation of power spectrum density (PSD) for ET, given the starting frequency ( $f_{low}$ ) and frequency steps ( $f_{\Delta}$ ). Second step is to generate a gaussian noise with a colour that matches the ET's PSD, sampled at the ET's frequency.

To generate GWs of a BBH sources, some parameters - of the source to be simulated - have to be provided, most importantly the masses of BBH and its  $D_L$ . These two parameters - for all our sources - were taken from Singh et al. (2021), which contains a physical properties (masses and redshift  $z$ ) of three populations of merging binaries (NSs and BHs) simulated specifically for the ET, using the ET-D design (Hild et al. 2011). To obtain  $D_L$  from redshift  $z$ , we used Planck 2015 cosmology (Planck Collaboration et al. 2016) assuming flat LCDM, with Hubble constant,  $H_0 = (67.8 \pm 0.9) \text{ km/s/Mpc}$ , a matter density parameter  $\Omega_m = 0.308 \pm 0.012$ , and a scalar spectral index with  $n_s = 0.968 \pm 0.006$ .

pyCBC also requires specifying the approximant, which is the model to be used for the simulation. We used *IMRPhenomD* approximant (Husa et al. 2016) which describes time and frequency domain GWs from non-precessing BBHs. More parameters as in Table 1 was to be provided, such as Positions in the sky, time steps ( $t_{\Delta}$ ), starting frequency ( $f_{low}$ ), Inclination angle ( $I_{\theta}$ ), Polarization ( $P_{\delta}$ ) and Coalescence ( $C_{\delta}$ ) phases. It must be noted here that, lower starting frequency will result in longer lasting waveforms that can last up to days on the detector. Since we are interested in detecting the BBHs' mergers, starting frequency was set to 30 Hz to have shorter waveforms.

## 2.1 Data processing

The output of the pyCBC simulation is a one channel time-domain data ( $d(t)$ , where  $d(t)$  is either a pure gaussian noise ( $n$ ) or has a signal ( $h$ ) been injected into it:

$$d(t) = \begin{cases} h(t) + n(t), & \text{if data contains a BBH's signal} \\ n(t), & \text{if data contains noise only.} \end{cases} \quad (1)$$

Using the parameters in Table 1, 25,000 BBH signals were generated with  $D_L$  up to 120 Gpc and five SNR ranges: 4-5,

PyCBC's parameter	Value
Detector	E1 detector
RA and Dec	Random (uniform distribution)
M1 and M2	$\in 15\text{-}56 M_{\odot}$
$D_L$	145-120,000 Mpc
$f_{low}$	30 Hz
$f_{\Delta}$	1.0/16
$t_{\Delta}$	1.0/16384
$I_{\theta}$	$\cos(\theta) = \text{uniform}[0, \pi]$
$P_{\delta}$	$\text{uniform}[0, 2\pi]$
$C_{\delta}$	$\text{uniform}[0, 2\pi]$

**Table 1.** Parameters for generating GWs BBH sources.

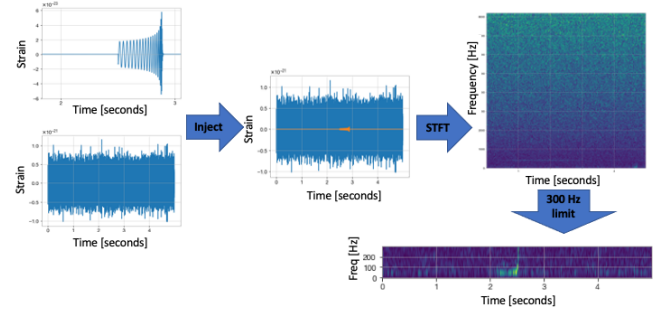


**Figure 1.** Data preparation and processing.

5-6, 6-7, 7-8 and  $>8$ . In ML, it's important to make sure the training data-set is well balanced, to make sure that classifiers won't be biased, in our case, towards a certain SNR range. To make sure that each SNR range has the same number of sources, we generated 180,000 BBH's signals and then divided them -based on their SNR values- into the five mentioned ranges. From each SNR range, 5000 signals were selected.

The data preparation and processing has four main steps as shown in Figure 1: (1) Signal and noise generation, generated signals has an observation time  $T$  ranges between 0.29 to 0.93 seconds, and each generated noise is a 5 seconds long. (2) Each signal was injected -in a random position- into the 5 seconds long noise. (3) STFT was used to produce the phase and magnitude spectrograms of each injection (noise plus signal) and a noise only time series. The result of this step is a spectrograms of only noise data (here after only noise spectrograms) and spectrograms of data with injected signals (here after injected spectrograms). (4) Limit the frequency to 300 Hz, this is due to the fact that, our signals are always at the bottom of the spectrograms, lies within the 300 Hz limit. This step saves time and computational power needed for the training since we are removing a significant part of the spectrogram where it's only noise. Figure 2 displays samples of only noise and injected spectrograms, where we show samples of 5 injected signals with SNR belong to the five ranges. We did not whiten the data and no bandpass filtering was applied. For the training of our CNN models, only the magnitude of the STFT was used and the complex part was ignored.

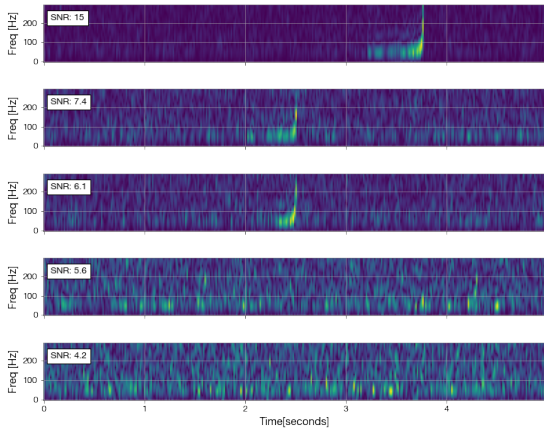


**Figure 2.** Injected spectrogram samples: top, and only noise spectrogram samples: bottom.

### 3 CONVOLUTIONAL NEURAL NETWORKS (CNN)

The Convolutional Neural Networks (ConvNet; Fukushima (1980)) is a type of feed-forward neural network deep learning model. A feed-forward model means the output from one layer will be used as an input to the subsequent layer. CNNs are primarily designed to take advantage of the 2D structure of an input image (or other 2D input such as a speech signal) to solve complex tasks such as pattern recognition and object detection (O’Shea & Nash 2015). CNNs have a multi-layer structure, which contains different layers with different rules. These layers namely are, convolutional layers, pooling layers and fully-connected layers, for details please see (Schmidhuber 2014). The main rule of a convolutional layer, is to extract features from the input (an image of a spectrogram in our case) through applying a user-defined number of filters, using a convolution operations (Goodfellow et al. 2016). Each convolutional layer is usually followed by an activation function -to introduce none-linearity in the model-

such as Hyperbolic Tangent  $\tanh$ ,  $\text{sigmoid}$  (Haykin 1998),  $\text{softmax}$  (Bridle 1990), or Rectified Linear Activation function ( $\text{ReLU}$ ) (Agarap 2018). A Pooling layer comes after the activation function and its main rule is to apply an scalar to vector transformation on a local regions of an image, to generate a representative value of the pixels in that region. Once the features have been pooled, it will be then flattened and fed to a fully connected layer. The rule of the fully-connected layer is same as Artificial Neural Networks (ANNs) which acts as a features classifier (Agarap 2017). CNNs are essentially made up of neurons that receive inputs. When training an CNNs model, the model will learn the associated features of each class, through minimizing the difference (loss) between output prediction and training true labels. For details please see (O’Shea & Nash 2015). In short, the CNNs process describes a none-linear mapping between the input images and their associated class scores.

#### 3.1 CNNs models

Our main task is to be able to distinguish whether a spectrogram has an injected signal or not, hence it’s a classification problem. In this work, we made use of the most popular networks in computer vision with the state-of-the-art performance in image classification and localization, to look for the most optimal model with the highest performance regarding the problem in hand. These models are namely VGG, ResNet and DenseNet networks.

##### 3.1.1 VGG network

First introduced in 2014 by (Simonyan & Zisserman 2014) in the ImageNet challenge, where their submission won the first and the second places in the localization and classification tracks respectively. They built 2 models with 16 and 19 convolutional layers with 3 by 3 kernel size. We used both architectures, VGG16 and VGG19, in this work.

##### 3.1.2 ResNet

Presented by He et al. (2015) on the ILSVRC 2015 classification challenge, where ResNet architecture won first place. ResNet uses batch normalization, which adjusts the input layer, and identity connection between the layers to protect the network from the well-known vanishing gradient problem. ResNet has different architectures which follow the same concept but with different number of layers, for example ResNet-18, ResNet-34, ResNet-50, ResNet-101, ResNet-110, ResNet-152 etc, we made use of ResNet-101 (ResNet hereafter).

##### 3.1.3 DenseNet

In DenseNet (Huang et al. 2016), the input does not only come from only the previous layer, but from all the preceding layers, which means all the preceding layers share their feature-maps to all subsequent layers. All layers are concatenated in DenseNet, which gives each layer an access to a collective knowledge from all the previous layers. DenseNet achieved higher accuracy compared to ResNet on ImageNet dataset. In this work, we used DenseNet-121 (DenseNet hereafter), which has 120 Convolutional and 4 AvgPool layers.

Type	Number of Sample	Train	Test	Val
Injected	25,000	17,000	4000	4000
Only noise	25,000	17,000	4000	4000
Total	50,000	34,000	8000	8000

**Table 2.** Total number of: injected and only noise spectrograms, training, testing and validation spectrograms.

### 3.2 Training

The performance of the ML models depend largely on the quality of the training data not on the algorithms (Zhao et al. 2015), which means different algorithms should provide generally similar trend if trained on a robust and large enough data. Hence we devoted a considerable effort to make sure our synthetic data is well representative in terms of  $D_L$ , mass distribution and balanced SNR ranges of all our BBH sources. We trained VGG16, VGG19, ResNet and DenseNet models with a batch size of 256, learning rate of 0.0001, 200 epochs using RSM optimizer. These parameters were chosen through running different experiments. The input layer size for all models were adjusted to  $42 \times 365 \times 1$  shape size which describe the width, height and number of bands of the input image respectively (1 band denotes gray scale images). As a tradition in training ML models, our data were split into training, validation and testing sets, Table 2 shows the total number of spectrograms used in each.

### 3.3 Networks Evaluation

To evaluate our trained models, a classification report was produced for each model for each SNR range where the precision, recall and F1-scores (Fawcett 2006) were calculated as shown in Table 3. In terms of accuracy, DenseNet, ResNet and VGG19 showed significantly better performance over VGG16, on sources with higher SNR ranges (6-7, 7-8 and  $>8$ ). DenseNet was outperformed by ResNet in SNR range 4-5 with 0.02, and VGG19 with 0.005 better accuracy score respectively. And in SNR range 6-7 by ResNet, with 0.01. In SNR range 7-8, DenseNet has better accuracy score with 0.02 over ResNet, and both has identical performance in SNR  $>8$  of 0.985. Same conclusion will be drawn if we compare the values of F1-score of both, ResNet and DensNet. Based on this, ResNet model was used for producing confusion matrix to further evaluate its performance. Better visualization of the accuracy for all models is shown in Figure 3 where the detection accuracy is compared to all SNR ranges for each models. The general trend is exactly as expected, where higher SNR sources have higher detection accuracy. It can clearly be seen that all models can detect completely hidden signals, with different accuracy, from sources with very low SNR down to 4.

Confusion matrix (Stehman 1997) illustrates how accurate the model is classifying each class, injected and only noise for each SNR range in our case, through visualizing the true positive, false positive, true negative and false negative values for each class. For producing confusion matrices, we have generated 200 spectrograms (of injected signals and only noise) for each SNR range. Figure 4 displays the confusion matrices for each SNR range. For SNR  $>8$ , no only-noise spectrogram

Model	SNR range	class	accuracy	precision	recall	f1-score
VGG16	4-5	injected	0.575	0.913	0.212	0.344
		noise		0.554	0.980	0.708
	5-6	injected	0.595	0.919	0.343	0.500
		noise		0.596	0.970	0.738
	6-7	injected	0.765	0.988	0.808	0.889
		noise		0.838	0.990	0.907
	7-8	injected	0.840	0.979	0.929	0.953
		noise		0.933	0.980	0.956
	$> 8$	injected	0.910	0.990	0.990	0.990
		noise		0.990	0.990	0.990
VGG19	4-5	injected	0.605	0.913	0.212	0.344
		noise		0.554	0.980	0.708
	5-6	injected	0.620	0.900	0.273	0.419
		noise		0.571	0.970	0.719
	6-7	injected	0.830	0.941	0.808	0.870
		noise		0.832	0.949	0.887
	7-8	injected	0.920	0.967	0.899	0.932
		noise		0.906	0.970	0.937
	$> 8$	injected	0.925	0.980	0.970	0.975
		noise		0.970	0.980	0.975
RESNET	4-5	injected	0.620	0.604	0.586	0.595
		noise		0.598	0.616	0.607
	5-6	injected	0.600	0.667	0.566	0.612
		noise		0.623	0.717	0.667
	6-7	injected	0.850	0.724	0.899	0.802
		noise		0.867	0.657	0.747
	7-8	injected	0.925	0.727	0.939	0.819
		noise		0.914	0.646	0.757
	$> 8$	injected	0.985	0.711	0.919	0.802
		noise		0.886	0.626	0.734
DENSENET	4-5	injected	0.600	0.919	0.343	0.500
		noise		0.596	0.970	0.738
	5-6	injected	0.605	0.865	0.455	0.596
		noise		0.630	0.929	0.751
	6-7	injected	0.845	0.958	0.919	0.938
		noise		0.922	0.960	0.941
	7-8	injected	0.945	0.990	0.990	0.990
		noise		0.990	0.990	0.990
	$> 8$	injected	0.985	0.980	1.000	0.990
		noise		1.000	0.980	0.990

**Table 3.** Evaluation metrics for all models.

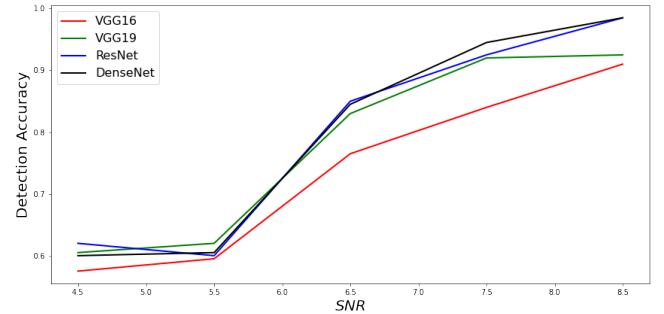


**Figure 3.** SNR versus detection's accuracy.

was classified as an injected one, while only one only-noise in SNR range 7-8 was miss-classified as an injection. 8 injected spectrograms were mis-classified as only-noise and 5 only-noise got classified as injected in SNR range 6-7. For SNR range 5-6, 54 injected spectrograms were classified as only-noise, while only 7 only-noise spectrograms were recognised as injected. The least performance was for SNR 4-5 sources, where 66 injected spectrograms were classified as only-noise, but only three injected spectrograms were classified as only-noise. This indicates a very good performance and means that type II error is unlikely to occur, therefore the model won't easily recognize noise as an injection.

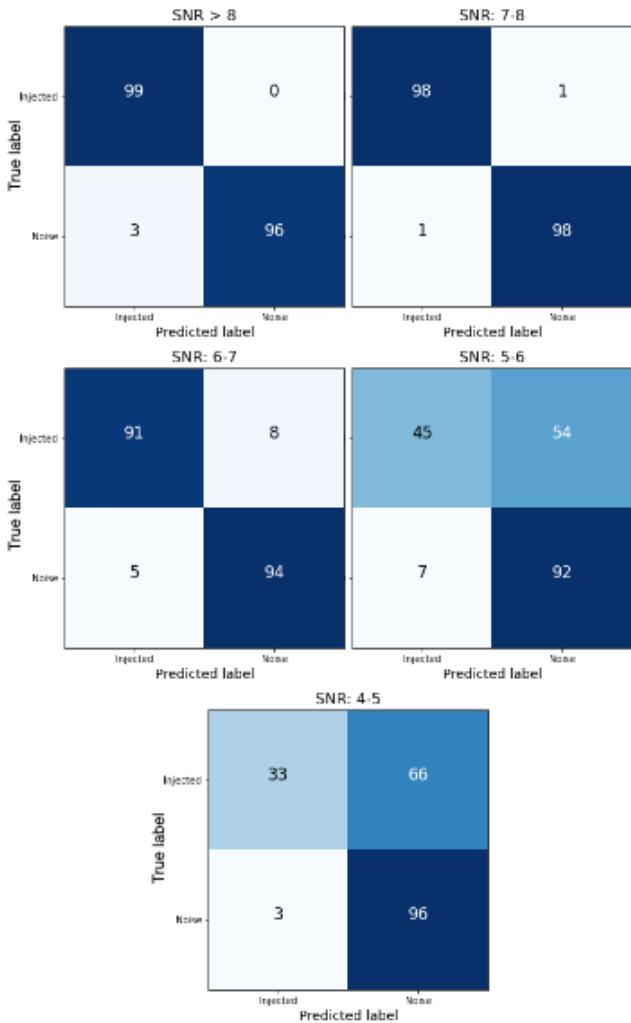


**Figure 4.** Confusion matrix for all SNR ranges.

#### 4 EVALUATION ON ET'S SYNTHETIC DATA

It's important to evaluate our best performing model on a relatively long time series data, to check for the efficiency and practicality of a near-real time detection. To do so, we generated a mock data of five hours and 75 seconds of time series data with a signal injected randomly in every five seconds, and one hour and 15 seconds data of only noise. False Alarm Rate (FAR) (also called false positive ratio or Type I Error Rate) is the ratio of the total number of false positive (FP) (here the number of undetected sources that's actually been injected but were miss-classified as pure noise) by the total number of FP and true negative (TN) (here the total number of injected sources). FAR is an effective metric for measuring the performance of machine learning models applied to classification problems (Burke et al. 1988). Mathematically it is calculated as:  $FP/(FP + TN)$ . Each segment (hour and 15 seconds) in the injected mock data contains 723 signals, which belong to specific SNR range. For the detection and calculation of FAR on this data, we built a pipeline where a sliding window of 5 seconds size will be moved through the data to capture a 5 seconds chunk each time. Then a spectrogram will be produced for each chunk and fed into

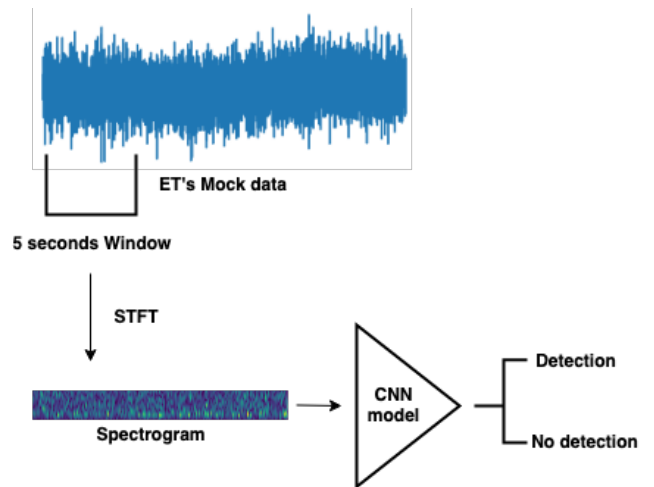


**Figure 5.** Inference on ET's synthetic data

Hours	SNR range	Total	Detected	FAR
1st	>8	723	722	0.001
2nd	7-8	723	713	0.014
3rd	6-7	723	687	0.050
4th	5-6	723	336	0.535
5th	4-5	723	208	0.712
6th	Noise only	0	24	0.033

**Table 4.** Detection evaluation on ET's synthetic data.

the model for inference. Figure 5 displays the flow chart of the ET's mock data inference process. Table 4 shows the report for each hour, where the number of detected sources is compared to the total number of injected signals, and FAR is calculated for each hour. 722 sources with SNR >8 out of 723 total sources were detected, with only 0.001 FAR. For sources with 7-8 SNR range, 713 sources were detected with an FAR of 0.014, while sources with 6-7 SNR range has an FAR of 0.05 with 687 sources detected. Sources with 5-6 and 4-5 SNR range have lower FAR as expected, with 336 and 208 sources were detected respectively. 24 nonexistent sources were detected in the only noise hour of data. This confusion is due to the training on signals with lower SNR. For instance, sources with SNR of 4 to 5 -on the spectrogram- would look identical to a pure noise once injected. When training an CNNs model on sources with SNR  $\geq 8$ , the model won't confuse a pure noise with signals. The confusion was very limited with only 0.033 FAR.

The scan of each hour from the data took 4 minutes and 57 seconds on an Core i7 MacBook Pro (with 16 GB memory, 2667 MHz DDR4 and 2.6 GHz processor) without parallelizing the code. This indicates that, the use of CNNs for merger detection is computationally efficient and can be significantly improved.

To further explore and evaluate the performance of the model, we plot the SNR,  $D_L$  and chirp mass  $M$  of the detected and undetected BBH sources. The chirp mass governs the motion and the waveform of the binary during the inspiral phase (Bulik & Belczynski 2003), and it depends on the individual masses  $m_1$  and  $m_2$  of the binary component, calcu-

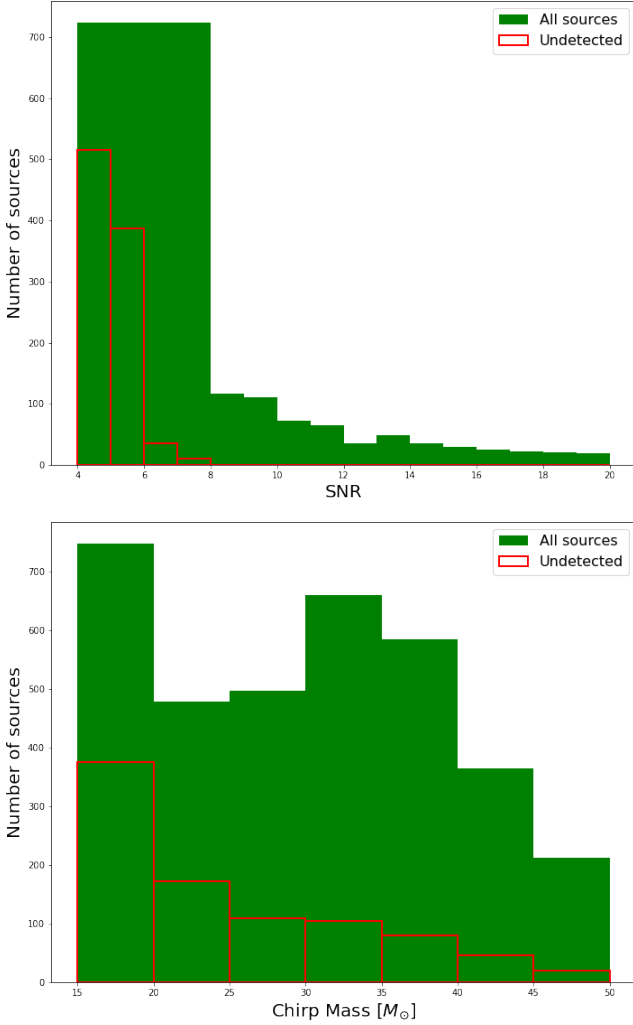


**Figure 6.** Top: SNR of all BBHs sources and the undetected ones. Bottom: Chirp mass of all BBHs sources and the undetected ones.

lated as  $M = (m_1 + m_2)^{-1/5} (m_1 \times m_2)^{3/5}$  (Peters & Mathews 1963).

Figure 6 and Figure 7 displays the SNR,  $M$  and  $D_L$  associated with the detected and undetected BBH sources respectively. Detected sources range in  $D_L$  from 125 - 60 Gpc, SNR from 4 - 168, and chirp mass from 15 - 56  $M_{\odot}$ . Undetected sources have a left skewed distribution for chirp mass and maximum  $D_L$  of 117,5 Mpc with SNR range between 4 to 8.8. Most undetected sources have lower SNR and mass with larger  $D_L$ . Minimum SNR detected source has an SNR of 4 with  $D_L$  of 17,9 Mpc and 23.6  $M$ , while the maximum  $D_L$  of a detected source has SNR of 4.3 with a  $D_L$  of 60 Gpc and  $M$  of 35  $M_{\odot}$ .

## 5 CONCLUSIONS AND FUTURE WORK

VGG16, VGG19, ResNet and DenseNet were trained and tested for the detection of BBHs merger from ET's synthetic data with five SNR ranges. Without performing data whitening or applying bandpass filtering, ResNet has significantly

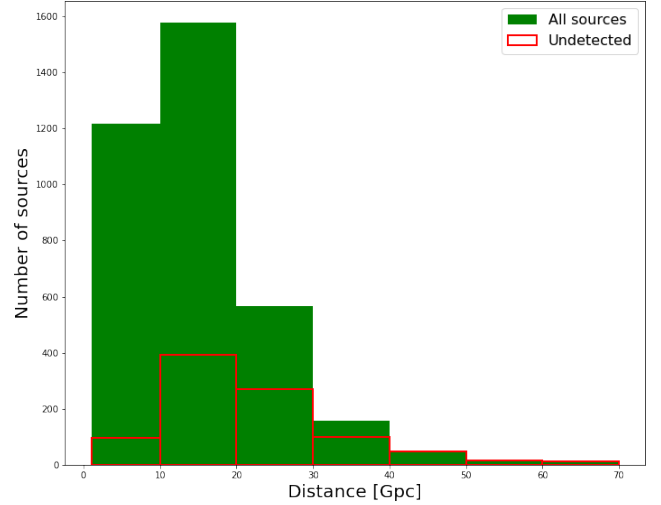


**Figure 7.**  $D_L$  of the all BBHs sources and the undetected ones.

better performance with an average accuracy of 85%. On testing data. ResNet model was able to detect BBHs sources with SNR of 8 or higher with 98.5% accuracy, and with 92.5%, 85%, 60% and 62% accuracy for sources with SNR range of 7-8, 6-7, 5-6 and 4-5 respectively. For 4-5 SNR range. ResNet model was able to detect a BBH's merger at 60Gpc with 4.3 SNR and a chirp mass of 35  $M_{\odot}$ . It was also shown that, the use of CNN for merger detection is computationally efficient, in our case, scanning a one hour of data only took 4 minutes and 57 seconds. This can be significantly improved, which makes our method -compared to matched filtering- more efficient for near-real-time detection. Future work will focus on spinning BBHs and BNSs sources, injecting glitches and consider the overlapped sources scenario.

## ACKNOWLEDGEMENTS

The authors thank Prof. Piotr Gawron and Dr. Josiah Ensign for their helpful discussions and reviews. This work has been supported by the DarkWave project (DarkWave H2020-WIDESPREAD-2018-2020 /H2020-WIDESPREAD-2020-5), and ‘‘AstroCeNT: Particle Astrophysics Science and Technology Centre’’ (MAB/2018/7) carried out within the International Research Agendas programme of the Foundation for Polish Science (FNP) financed by the European Union under the European Regional Development Fund. Additionally it made use of the computational cluster available at Nicolaus Copernicus Astronomical Center.

## DATA AVAILABILITY

Data used in this work -including time-series and spectrograms- can be shared on a reasonable request, please contact the author to request the data.

## REFERENCES

- Abbott B. P., et al., 2009, *Reports on Progress in Physics*, 72, 076901
- Abbott B. P., et al., 2016, *Phys. Rev. Lett.*, 116, 061102
- Abernathy M., et al., 2011, *Uniwersytet śląski*, pp 343–354
- Acernese F., et al., 2007, *AIP Conference Proceedings*, 924, 187
- Agarap A. F., 2017, arXiv e-prints, p. [arXiv:1712.03541](https://arxiv.org/abs/1712.03541)
- Agarap A. F., 2018, arXiv e-prints, p. [arXiv:1803.08375](https://arxiv.org/abs/1803.08375)
- Alhassan W., Taylor A. R., Vaccari M., 2018, *Monthly Notices of the Royal Astronomical Society*
- Álvarez J. D., Font J. A., Freitas F. F., Freitas O. G., Morais A. P., Nunes S., Onofre A., Torres-Forné A., 2021, *Classical and Quantum Gravity*, 38, 155010
- Baltus G., Janquart J., Lopez M., Reza A., Cudill S., Cudell J.-R., 2021, *Phys. Rev. D*, 103, 102003
- Baltus G., Janquart J., Lopez M., Narola H., Cudell J.-R., 2022, arXiv e-prints, p. [arXiv:2205.04750](https://arxiv.org/abs/2205.04750)
- Biswas R., et al., 2013, *Phys. Rev. D*, 88, 062003
- Blackman R. B., Tukey J. W., 1958, *The Bell System Technical Journal*, 37, 185
- Bonfield D., Sun Y., Davey N., Jarvis M., Abdalla F., Banerji M., Adams R., 2010, *Monthly Notices of the Royal Astronomical Society*, 405, 987
- Bridle J. S., 1990, in Soulié F. F., Héroult J., eds, *Neurocomputing*. Springer Berlin Heidelberg, Berlin, Heidelberg, pp 227–236
- Bulik T., Belczynski K., 2003, *The Astrophysical Journal*, 589, L37
- Burke D. S., Brundage J. F., Redfield R. R., Damato J. J., Schable C. A., Putman P., Visintine R., Kim H. I., 1988, *New England Journal of Medicine*, 319, 961
- Colgan R. E., Corley K. R., Lau Y., Bartos I., Wright J. N., Márka Z., Márka S., 2020, *Phys. Rev. D*, 101, 102003
- Collister A. A., Lahav O., 2004, *Publications of the Astronomical Society of the Pacific*, 116, 345
- D’Isanto A., Polsterer K. L., 2018, *Astronomy & Astrophysics*, 609, A111
- Evans M., et al., 2021, arXiv e-prints, p. [arXiv:2109.09882](https://arxiv.org/abs/2109.09882)
- Fawcett T., 2006, *Pattern Recognition Letters*, 27, 861
- Fukushima K., 1980, *Biological Cybernetics*, 36, 193
- Goodfellow I., Bengio Y., Courville A., 2016, *Deep Learning*. MIT Press
- Haykin S., 1998, *Neural Networks: A Comprehensive Foundation*, 2nd edn. Prentice Hall PTR, USA
- He K., Zhang X., Ren S., Sun J., 2015, *Deep Residual Learning for Image Recognition*, doi:10.48550/ARXIV.1512.03385, <https://arxiv.org/abs/1512.03385>
- Hild S., et al., 2011, *Class. Quant. Grav.*, 28, 094013
- Huang G., Liu Z., van der Maaten L., Weinberger K. Q., 2016, *Densely Connected Convolutional Networks*, doi:10.48550/ARXIV.1608.06993, <https://arxiv.org/abs/1608.06993>
- Husa S., Khan S., Hannam M., Pürrer M., Ohme F., Forteza X. J., Bohé A., 2016, *Phys. Rev. D*, 93, 044006
- Iacovelli F., Mancarella M., Foffa S., Maggiore M., 2022, arXiv e-prints, p. [arXiv:2207.02771](https://arxiv.org/abs/2207.02771)
- Jiang M.-Q., Yang N., Li J., 2022, *Frontiers of Physics*, 17, 54501
- Kalogera V., et al., 2021, arXiv e-prints, p. [arXiv:2111.06990](https://arxiv.org/abs/2111.06990)
- Kim E. J., Brunner R. J., 2017, *Monthly Notices of the Royal Astronomical Society*, 464, 4463
- Klimenko S., et al., 2016, *Phys. Rev. D*, 93, 042004
- Lukic V., Brüggem M., 2016, *Proceedings of the International Astronomical Union*, 12, 217
- Maggiore M., et al., 2020, *J. Cosmology Astropart. Phys.*, 2020, 050
- Moreno E. A., Borzyszkowski B., Pierini M., Vlimant J.-R., Spiropulu M., 2022, *Machine Learning: Science and Technology*, 3, 025001
- Naim A., Ratnatunga K. U., Griffiths R. E., 1997, *The Astrophysical Journal*, 476, 510
- Nitz A., et al., 2022, gwastro/pycbc: Release v2.0.1 of PyCBC, doi:10.5281/zenodo.5825666, <https://doi.org/10.5281/zenodo.5825666>
- O’Shea K., Nash R., 2015, arXiv e-prints, p. [arXiv:1511.08458](https://arxiv.org/abs/1511.08458)
- Peters P. C., Mathews J., 1963, *Phys. Rev.*, 131, 435
- Planck Collaboration et al., 2016, *A&A*, 594, A13
- Punturo M., Abernathy M., Acernese F., other 2010, *Classical and Quantum Gravity*, 27, 194002
- Schmidhuber J., 2014, arXiv e-prints, p. [arXiv:1404.7828](https://arxiv.org/abs/1404.7828)
- Schmidt S., et al., 2020, *arXiv: General Relativity and Quantum Cosmology*
- Selim I. M., Abd El Aziz M., 2017, *Experimental Astronomy*, 43, 131
- Selim I., E. A., M.El B., 2016, *International Journal of Computer Applications*, 137, 4
- Shaddock D. A., 2008, *Classical and Quantum Gravity*, 25, 114012
- Simonyan K., Zisserman A., 2014, *Very Deep Convolutional Networks for Large-Scale Image Recognition*, doi:10.48550/ARXIV.1409.1556, <https://arxiv.org/abs/1409.1556>
- Singh N., Bulik T., Belczynski K., Askar A., 2021, arXiv e-prints, p. [arXiv:2112.04058](https://arxiv.org/abs/2112.04058)
- Stehman S. V., 1997, *Remote Sensing of Environment*, 62, 77
- Vajente G., 2022, *Phys. Rev. D*, 105, 102005
- Willke B., 2007, *Classical and Quantum Gravity*, 24, S389
- Yin Q., Shen L., Lu M., Wang X., Liu Z., 2013, *Journal of Systems Engineering and Electronics*, 24, 26
- Zhang Y., Li L., Zhao Y., 2009, *Monthly Notices of the Royal Astronomical Society*, 392, 233
- Zhang X.-T., Messenger C., Korsakova N., Chan M. L., Hu Y.-M., Zhang J.-d., 2022, *Phys. Rev. D*, 105, 123027
- Zhao T., Jayaram V., Roy A., Marfurt K. J., 2015, *Interpretation*, 3, SAE29

This paper has been typeset from a  $\text{\TeX}/\text{\LaTeX}$  file prepared by the author.